Molecular design of responsive fluids: molecular dynamics studies of viscoelastic surfactant solutions

E S Boek[1], A Jusufi[1,2], H Löwen[2] and G C Maitland[1]

[1] Schlumberger Cambridge Research, High Cross, Madingley Road, Cambridge CB3 0EL, UK
[2] Institut für Theoretische Physik II, Heinrich-Heine-Universität Düsseldorf, Germany

E-mail: boek@cambridge.oilfield.slb.com

Abstract
Understanding how macroscopic properties depend on intermolecular interactions for complex fluid systems is an enormous challenge in statistical mechanics. This issue is of particular importance for designing optimal industrial fluid formulations such as responsive oilfield fluids, based on viscoelastic surfactant solutions. We have carried out extensive molecular dynamics simulations, resolving the full chemical details in order to study how the structure of the lamellar phase of viscoelastic surfactant solutions depends on the head group (HG) chemistry of the surfactant. In particular, we consider anionic carboxylate and quaternary ammonium HGs with erucyl tails in aqueous solutions together with their sodium and chloride counterions at room temperature. We find a strong HG dependence of the lamellar structure as characterized by suitable pair correlation functions and density distributions. The depth of penetration of water into the bilayer membrane, the nature of counterion condensation on the HGs and even the order and correlation of the tails in the lamellae depend sensitively on the chemical details of the HG. We also determine the compressibility of the lamellar system as a first step to using atom-resolved molecular dynamics in order to link the molecular and macroscopic scales of length and time. The results give important insight into the links between molecular details and surfactant phase structure which is being exploited to develop more systematic procedures for the molecular design and formulation of industrial systems.

(Some figures in this article are in colour only in the electronic version)

1. Introduction

The rich phase behaviour, rheological diversity and responsiveness to a variety of chemical and physical triggers exhibited by colloidal and polymeric liquids make them ideal building blocks for a wide variety of commercial fluids. Applications as diverse as in personal products,
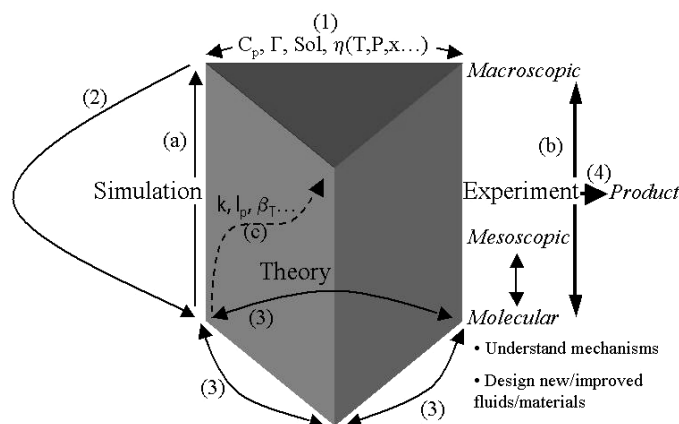
Figure 1. A schematic diagram of a systematic fluid formulation process: the integrated use of experiment, theory and simulation on a wide range of length scales. (1) Macroscopic process simulation specifies the optimum bulk properties required (e.g. heat capacity C_p, adsorption isotherm Γ, solubility 'Sol', viscosity $\eta(T, P, x)$). (2) Appropriate molecular and/or mesoscopic components are identified and optimized by use of experiment, theory and simulation in appropriate combination (3) to both allow an understanding of mechanisms and design new/improved fluids and materials. Links from the molecular/mesoscopic to the macroscopic are achieved by (a) direct simulation (for simple systems only at present), (b) experiment or (c) simulating phenomenological parameters in bulk theories such as bending modulus κ, persistence length l_p and isothermal compressibility β_T. The process identifies the most promising areas of parameter space, reducing the amount of experimentation required for final optimization (4) by an order of magnitude or more.

processed foodstuffs, agrochemicals, printing inks, oilfield stimulation fluids, cosmetics and coatings all utilize liquids or soft solids based on such components to achieve the multifunctional properties usually required in their use. To meet the specific demands of each application, such commercial liquids are usually multicomponent, multiphase and complex in composition, structure and dynamical behaviour. Their design involves an equally complex formulation process, in which the number of parameters (composition, conditions of manufacturing, storage, use and disposal) is so large that the approach is often empirical and far from optimized.

By contrast, the physics and chemistry of liquids is concerned with understanding the relationships between the nature and interactions of their fundamental building blocks and their bulk behaviour. Techniques—experimental, theoretical and simulation—have been evolved to link fluid composition, through molecular/mesoscopic interactions and their consequences for liquid structure over a range of length scales, ultimately to bulk thermodynamic and transport properties. Whilst this tripartite attack on the mysteries of the liquid state is most fully developed for relatively simple molecules and colloids, in terms of shape, flexibility, reactivity etc, it is being applied successfully to increasingly complex systems. Molecular design and the broader concept of fluids engineering seek to exploit this growing capability by inverting this process (see figure 1). The aim is to use realistic macroscopic process simulation models to specify the optimum fluid thermophysical properties required for a given application, as a function of all the key process parameters: temperature, pressure, time, ... Using the interactions–structure–property relationships established by a judicious combination of theoretical models, simulations and experiments on a wide range of length scales, the molecular or colloidal options for achieving these property specifications are identified and

the optimal compositions are defined. In other words the ability to model, simulate and experimentally probe liquids of increasing complexity opens up the prospect of a systematic framework/methodology for product formulation and the opportunity to turn the formulation activity from an empirical art to a systematic science.

This is an ambitious goal, of course, yet such techniques are being increasingly used to accelerate and optimize the industrial product development process. For oilfield applications, for instance, they have been used to identify classes of molecular components and specific types of structure that should lead to new or enhanced performance, leading to a small number of viable options for the final experimental optimization process. One example is the use of molecular mechanics simulations to design retarders to delay the hydration of cement slurries [1]. Here the adsorption of polyphosphonate species to block potential sulphate sites on the fast-growing faces of calcium–aluminium sulphate mineral intermediates delayed the onset of crystallization and prolonged the lifetime of protective gel layers coating the cement particles. Molecules with spatial arrangements of the phosphonate groups optimized to best match the geometric and charge density requirements of the hydrating mineral surface were found to give enhanced performance. Such molecular docking simulations depend more on geometric and charge matching rather than the subtle details of molecular interactions and have been applied to similar molecular design problems such as mineral scale growth inhibition [2] and crystal habit modification [3]. A more demanding application is in the design of oligomers capable of adsorbing from aqueous drilling fluids onto smectite clays in weak shale rocks, forming stabilizing adsorbed layers which prevent clay swelling by uptake of water. Molecular simulations played a key role in elucidating the underlying mechanisms of clay swelling [4] and in optimizing oligomer structures for optimum drilling performance [5].

Here we address a more ambitious problem. There is increasing need in hydrocarbon recovery processes for multifunctional, responsive fluids which can transform their characteristics (for example, from low-viscosity, Newtonian behaviour to those of a highly viscoelastic gel then back to those of a low-viscosity liquid) at different stages of a reservoir treatment process in response to chemical or physical triggers that either occur naturally in the process or can be imposed externally. Surfactant self-assembly and disassembly is one route for achieving this and viscoelastic surfactants (VESs) operating in the wormlike micelle regime are being increasingly used as reservoir stimulation fluids. This paper describes the use of molecular dynamics simulations to improve the understanding of the structure and stability of the surfactant phase, and the first steps in exploiting this understanding for optimizing surfactant molecular structure for enhanced performance. Surfactant self-assembly is more challenging than the earlier formulation examples because it involves larger molecular systems and longer timescales, challenging the limits of memory and speed of existing computer systems. Moreover, the problem is more sensitive to the details of molecular interactions than is molecular docking on surfaces, so due regard for the consequences of the inevitable uncertainties and simplifications in the interaction energy models used is essential.

The nature of the oilfield applications and of the VES fluids will first be described [6]. Then, given that MD simulations can only simulate such complex fluids for a few nanoseconds at most, we describe our approach for bridging the scales of time and length required to predict their bulk behaviour. The main focus of this paper is to investigate the consequences for micelle structure and stability of changes in head group (HG) structure which are known through experiment to have a dramatic impact on phase stability and rheological behaviour. The model used to simulate the lamellar phase will be described and MD results presented, showing how the nature and structure of the surfactant membrane change significantly with relatively small modifications to HG structure. The results are compared with earlier conclusions from coarser-grained simulations for cylindrical and spherical micelles of similar surfactants. Finally, the
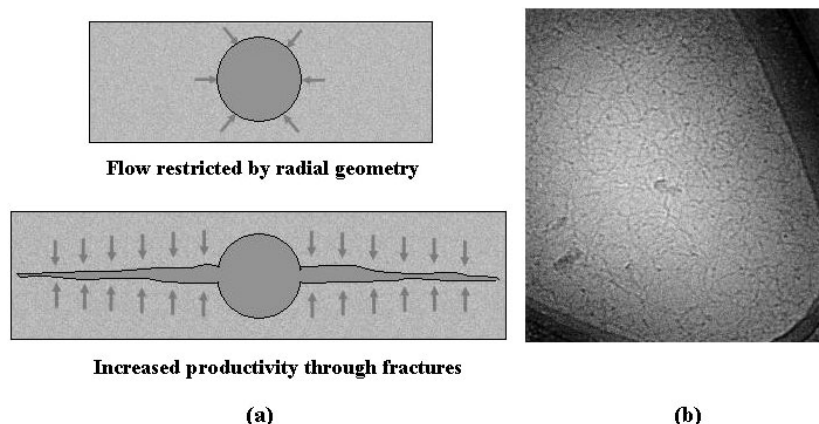
Figure 2. (a) A schematic diagram of an oil well in cross-section illustrating (top) how oil production can be limited due to radial flow into the well. The hydraulic creation of two opposing vertical fractures (bottom) extending up to 300 m from the well gives large productivity increases due to linear flow into the highly conductive fracture. This is propped open by sand transported into the fracture during its creation by the viscoelastic fracturing fluid, preventing closure when the pressure is reduced and production begins. The permeability of this packed bed is crucial to the enhancement of oil production. (b) A cryo-TEM image of the wormlike micelle structure obtained for a 4% v /v C22 quaternary ammonium cationic surfactant (EHAC; see the text) in 3% ammonium chloride, typical of the VES systems being used as fracturing fluids. This structure breaks down to spherical microemulsions as hydrocarbon is produced through the proppant pack.

consequences of the study for the optimal design of VES fluids, and future work to improve this molecular design process, will be discussed.

2. Oilfield applications and fluid requirements for VES fluids

Once an oil well has been constructed, its production can be limited by low natural reservoir permeability or by permeability reductions induced by particulate damage to the rock pore space during either drilling or production. The creation of hydraulic fractures is one major stimulation process commonly used to overcome these limitations.

The most common fracturing fluids use natural polymers, such as guar [7], cross-linked by borate or transition metal (Zr, Ti) complexes to form viscoelastic gels. These fluids transmit hydraulic pressure to the rock to induce fractures in the formation, into which sand or other ceramic particles ('proppant') are transported by the gel to give a porous proppant pack which keeps the fractures open on removal of the fluid pressure (see figure 2(a)). Once the proppant is in place, delayed oxidative or enzymatic breakers are used to degrade the gel retained within the proppant pack.

A serious limitation of many of these polymeric fluids is that, despite the gel-breaking step, small cross-linked fragments comparable in size to the sand-pack pore throats reduce the hydraulic conductivity of the pack significantly. A new generation of fracturing fluids based upon VESs has recently been introduced [6] which attempts to address this problem. Their gel rheology is caused by wormlike cylindrical micelles (see figure 2(b)). Once these come into contact with hydrocarbon produced from the fracture through the proppant pack, they revert to small spherical micelles or microemulsions [8], the fluid viscosity/elasticity falls by orders of magnitude, the fluid residues flow easily out of the pack and fracture flow-back efficiencies of close to 100% are achieved.
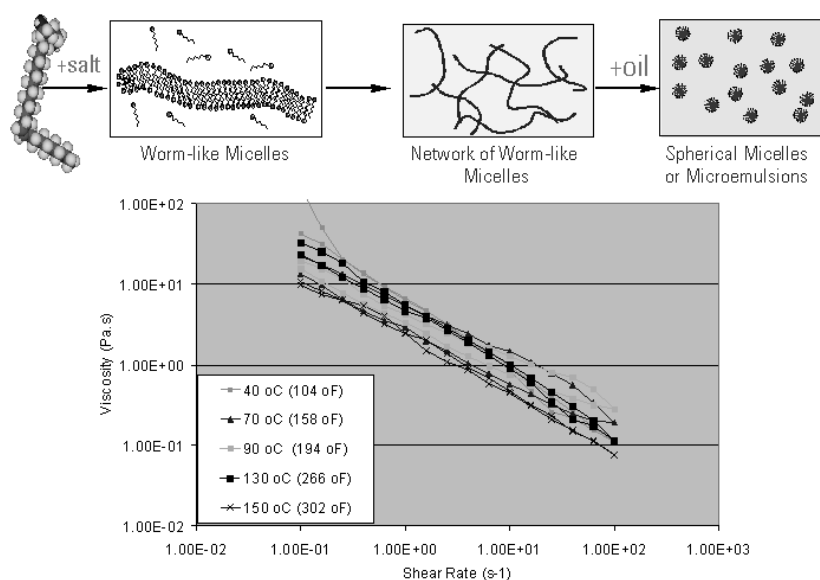
Figure 3. A schematic diagram of the production of wormlike micelles, their destruction by oil and the rheology of a dilute solution (typically 2% w/w) that results from such structural changes.

Recent studies of microstructure [9, 10] and rheology [11, 12] for model wormlike micelle-forming systems such as CTAB provide the underpinning understanding of molecular–bulk property relationships to guide fluid design. Of particular significance for controlling applications is the strong coupling between shear flow and structure/phase behaviour for these systems [13]. Molecular [14, 15] and mesoscopic [16] simulations are also proving successful at probing these relationships. The general rheological behaviour of VESs comprising wormlike micelles can be rationalized within the now classical framework of Cates [17].

The principle of VES fracturing fluids is shown in figure 3. The surfactant, typically a C22 erucyl derivative, is activated by salt, which screens the HG charge interactions, to form wormlike micelles. These form a highly entangled network, giving rise to a high-viscosity, dramatically shear-thinning and elastic solution at relatively low (<5 wt%, $\sim$10–100 mM) surfactant concentrations. Typical length scales for the system are: micelle contour length 900 nm, micellar radius 2 nm, entanglement length 300 nm, micelle persistence length 200 nm. Exposure to oil, typically $\sim$1 wt%, causes the micelles to revert to spherical microemulsions with viscosities close to that of water. Raghavan and Kaler [18] recently published a definitive study of the rheological behaviour of EHAC (erucyl bis(2-hydroxyethyl) methylammonium chloride) which demonstrates the characteristics typical of this type of fluid. Several features are important. The low-shear viscosity decreases exponentially with temperature, as does the relaxation time ($\sim 1/\gamma_c$) characterizing the onset of shear-thinning. In contrast, the viscosity at high shear rates (above γ_c) is essentially independent of temperature (see for example figure 3), as is the shear-thinning power law index (~ -1). The wormlike micelle regime can be activated by non-binding salts, like sodium chloride, where fluid viscosity goes through a maximum with salt concentration.

For oilfield applications, the ability to sustain high temperatures is particularly important. One design criterion is that the viscosity at a shear rate of $100\,\mathrm{s}^{-1}$ must be greater than 50 mPa s. Changes in HG chemistry can markedly affect the temperature at which this fails to be achieved.

EHAC is limited to temperatures below 85 °C, whereas replacing the hydroxyethyl groups by methyl reduces this temperature to about 70 °C [19]. By contrast, replacing the quaternary cationic HG by the smaller anionic carboxylate group increases this critical temperature to over 100 °C.

A major objective of the current study is to understand why these relatively small changes in HG structure cause such major changes in high-temperature rheology and, by inference, the stability of the wormlike phase. To do this by molecular simulation, clearly an all-atom approach incorporating all the molecular detail of the surfactant chain is essential, as it is in this detail that the origin of the dramatic bulk property changes reside. Yet MD calculations for the size of system needed to give a realistic model (at least 100 surfactant chains and an order of magnitude more water molecules) can only reach a few nanoseconds in overall timescale. This means that the direct evaluation of transport coefficients through calculation of the relevant time correlation functions [19] or via NEMD approaches [20] is out of the question. Even the full evolution of spontaneous micelle growth and exchange of surfactant molecules between micelles and bulk solution cannot yet be studied [21]. An alternative approach is therefore needed to bridge the gap between MD simulation and bulk behaviour.

3. Bridging the molecular and bulk scales of length and time

A possible approach to understanding the bulk behaviour of surfactant systems as one changes molecular structure is to use molecular dynamics to evaluate parameters that appear in phenomenological approaches. For instance, the well established approach of Helfrich [22], Safran [23] and co-workers expresses the phase behaviour of surfactant systems in terms of the characteristic macroscopic parameters spontaneous curvature, bending modulus and saddle-splay modulus. If these parameters can be evaluated by molecular simulation, then changes in phase behaviour (lamellae–cylindrical–spherical micellar) due to molecular variations may be accessible. One route is to derive the bending modulus κ from the wavelength dependence of spontaneous shape fluctuations of the lamellar phase. This has been done for highly coarse-grained bead–spring models [24] as well as atomistic surfactant models [25, 26]. An alternative route is via the isothermal compressibility, β_T, since for elastic rods of radius R [27],

$$\kappa = \tfrac{1}{4}\pi E R^4, \tag{1}$$

where $E \approx 3/\beta_T$ in the limit of $\kappa \ll \mu$, where μ is the torsion modulus. Ben-Shaul *et al* [28] have shown that the persistence length of a wormlike micelle, l_p, is related to the bending modulus κ by the expression

$$l_p = \frac{\kappa}{k_B T}. \tag{2}$$

This provides an alternative route to the phenomenological phase maps, and also a link to the micelle dynamics and rheology via the Cates model [17] and its recent extensions.

Since simulation of the bilayer membrane provides a route into the bending moduli of a surfactant system, this phase was selected for the initial MD study because it also has a number of operational advantages. The planar surface is easier to analyse than a cylinder and the smaller surface area per HG means that fewer water molecules are needed. As we shall see, the membrane structure turns out to show similar features to that of cylindrical and spherical micelles simulated using a coarser-grained model for similar anionic carboxylate surfactants [29].

4. Surfactants studied

In our studies, two types of surfactant were investigated, which differ in their hydrophilic HG chemistry. Their tails are consistently erucyl chains, chemically described as $(CH_2)_{12}$–$CH=CH$–$(CH_2)_7$–CH_3. In some cases the tail was chopped at the double-bond section. The surfactants have ionic HGs of the following types:

- **erucate**: anionic surfactant with a carboxylate HG ($-COO^-$).
- **EHAC**: cationic surfactant with $-N^+$ ($CH_2CH_2OH)_2CH_3$ (bis(hydroxyethyl) methylammonium) HG.

In order to study the membrane surface structure, the centre of mass of the HG is calculated from its atomic constituents. Its radius of gyration R_g is taken as a measure for the spatial extent of the HG. The radius of gyration is simply defined as the mean distance of all HG atoms from their common centre of mass:

$$R_g = \frac{1}{N} \sum_{i=1}^{N} (\vec{r}_i - \vec{R}_{cm})^2, \tag{3}$$

where $\vec{r}_i$ is the position of one of the N atoms in the HG, and $\vec{R}_{cm}$ is the position vector of the centre of mass of the HG, given by

$$\vec{R}_{cm} = \frac{1}{M} \sum_{i=1}^{N} m_i \vec{r}_i. \tag{4}$$

m_i denotes the mass of HG atom i and $M = \sum_{i=1}^{N} m_i$ is the HG mass.

5. Simulation model

Our simulation model consists of a double layer of surfactant molecules, counterions $((Na^+)^3$, or $(Cl^-)^4)$ and water molecules. For water, the simple point charge (SPC) model was used [30]. Non-bonded interactions between ions, solvent and surfactants are pairwise additive and consist of electrostatic and Lennard-Jones 6–12 potential terms:

$$v = \sum_{i<j} (q_i q_j / r_{ij} - D_{ij}/r_{ij}^6 + E_{ij}/r_{ij}^{12}). \tag{5}$$

The methylene ($>CH_2$) and methyl ($-CH_3$) groups of the hydrocarbon tail were treated using an all-atom model that explicitly includes H atoms. All-atom models are considered to have certain advantages over pseudoatom models, which do not treat H atoms explicitly [29].

We used the open-source MD simulation package DL_POLY [34], which has a number of choices for intramolecular potentials. We used the following potential functions for the bonded particles:

- the harmonic bond potential:

$$U(r_{ij}) = \tfrac{1}{2} k (r_{ij} - r_0)^2, \tag{6}$$

with r_{ij} being the distance between two particles labelled i and j. k and r_0 are the bending constant and the mean distance, respectively;

---

[3] In the erucate case.
[4] In the EHAC case.

Table 1. A list of fractional charges of the HG atoms calculated with the MOPAC algorithm for both EHAC and erucate surfactants. The index of the atoms corresponds to the subgroups in the HG structure. Note that the MOPAC charges of the atoms in the hydroxyethyl subgroup, which occurs twice in the EHAC HG, are very similar, and therefore the average atomic charges are given. The atomic charges in this subgroup are listed according to the distance to the nitrogen atom.

EHAC HG atom	q_i/e	Erucate HG atom	q_i/e
N^+	0.04	C_{COO^-}	0.32
		O_{COO^-}	−0.59
C_{CH_3}	−0.17	O_{COO^-}	−0.60
H_{CH_3}	0.15	Total	−0.87
H_{CH_3}	0.14		
H_{CH_3}	0.15		
C_{CH_2}	−0.13		
H_{CH_2}	0.14		
H_{CH_2}	0.14		
C_{CH_2}	−0.03		
H_{CH_2}	0.11		
H_{CH_2}	0.09		
O_{OH}	−0.34		
H_{OH}	0.24		
Total	0.75		

- the valence angle potential:

$$U_\Theta(\Theta_{ijk}) = \frac{k_\Theta}{2}(\cos(\Theta_{ijk}) - \cos(\Theta_0))^2, \tag{7}$$

where Θ_{ijk} denotes the angle between three bonded atoms (k_Θ and Θ_0 are the bending constant and the mean angle, respectively);

- the dihedral angle potential:

$$U_{di}(\Phi_{ijkn}) = A[1 + \cos(m\Phi_{ijkn} - \delta)], \tag{8}$$

with Φ_{ijkn} being the dihedral angle defined by

$$\Phi_{ijkn} = \arccos(B(\vec{r}_{ij}, \vec{r}_{jk}, \vec{r}_{kn}))$$

$$B(\vec{r}_{ij}, \vec{r}_{jk}, \vec{r}_{kn}) = \frac{(\vec{r}_{ij} \times \vec{r}_{jk}) \cdot (\vec{r}_{jk} \times \vec{r}_{kn})}{|\vec{r}_{ij} \times \vec{r}_{jk}||\vec{r}_{jk} \times \vec{r}_{kn}|}.$$

A and δ are constants and m is an integer.

All intramolecular and van der Waals parameters in equations (5)–(8) are extracted from the Dreiding force field [31].

The SPC water molecules are modelled by the method of constraints, using the SHAKE algorithm [20]. The O–H bond is constrained at 1.0 Å, whereas the H–H distance is constrained at 1.63 Å.

In addition, we take the atomic charges into account. In the SPC water model the oxygen and hydrogen atoms have fractional charges of −0.82 and 0.41 e respectively. The monovalent counterions carry their full charge. The charges on the surfactant atoms were determined using a MOPAC [32] simulation of a single molecule *in vacuo*; table 1 shows a list of the fractional charges for the HG atoms as calculated with this semi-empirical quantum chemical method. Note that the formal charges of the surfactants are +1 and −1 for the EHAC and the erucate, respectively. It appears that the MOPAC calculations assign net charges of +0.75 and −0.87
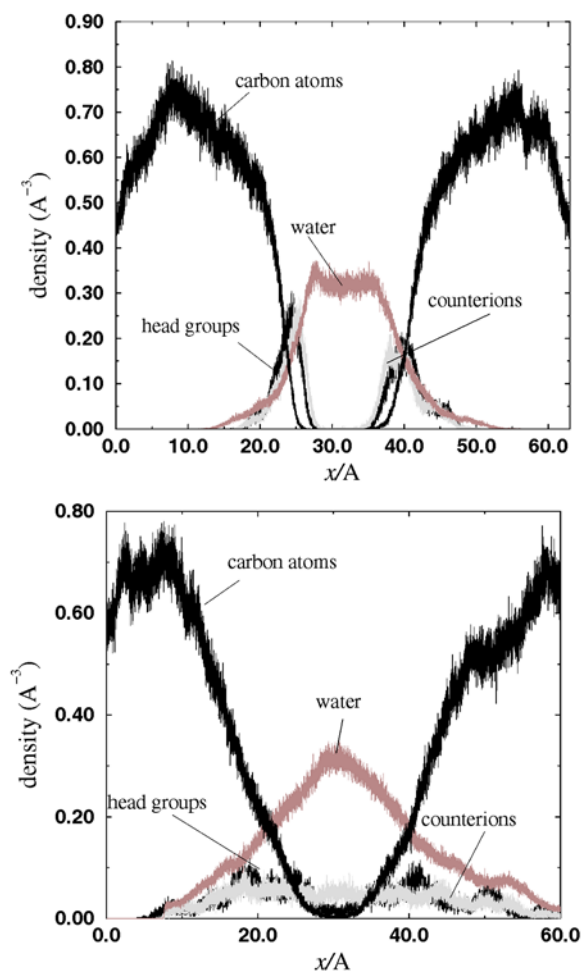
Figure 4. Density profiles of HGs, counterions, water molecules and carbon atoms for both erucate (top) and EHAC (bottom). Note that the dip in the density profile of the erucate carbon atoms near $x = 0$ and 60 Å is an artefact of the constant-pressure algorithm (volume fluctuations) and has no physical meaning.

to the EHAC and erucate HGs respectively; this means that the remaining charges (+0.25 and −0.13, respectively) are distributed along the hydrocarbon chains. This means that the net charges of the two surfactant tails will be slightly different. Note that this is only an artifact of the MOPAC calculations and has no physical significance. In order to check the effect of having a small net charge on the hydrocarbon chains, we have performed the same simulations with an uncharged surfactant tail (and net HG charges of +1 and −1 for the EHAC and erucate respectively). It appears that the differences in the observed membrane structures, as characterized by the radial distribution functions $g_{ij}(r)$ and density profiles described in section 7, are insignificant. As an illustration, the carbon–carbon $g(r)$ is shown for both the uncharged and the charged chain models in figure 7. A full analysis of the residual charge effects will be described elsewhere [33].
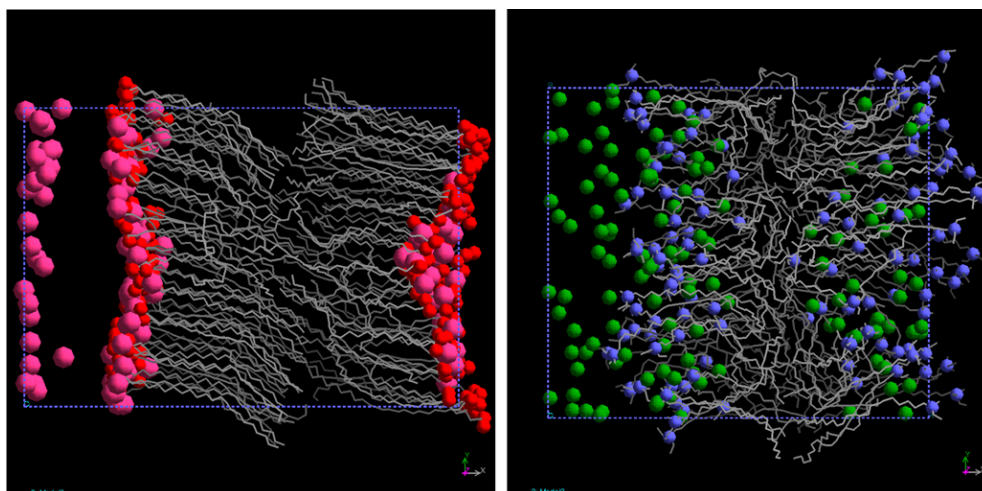
**Figure 5.** Simulation snapshots of HGs, tails and counterions for both erucate (left) and EHAC (right).
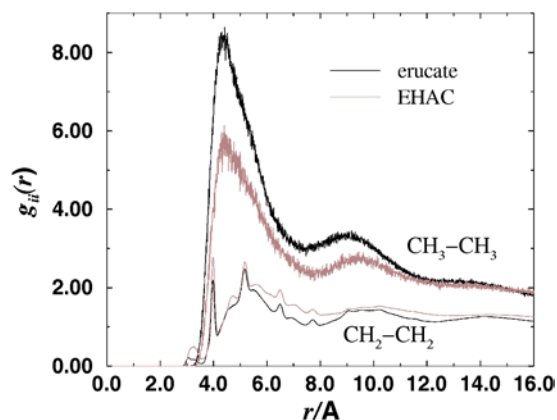
Figure 6. The pair correlation function $g_{ii}(r)$ for the $i = CH_2$ carbon atoms (lower curves) and the $i = CH_3$ carbon atoms (upper curves), shown for both erucate (black) and EHAC (grey) 8×8 surfactant bilayer systems.

6. Details of the MD simulations

Our simulations were performed using the parallel MD code DL_POLY [34]. The calculations were performed on an SGI Origin2000 computer server equipped with 32 R10000 processors. The MD cell has orthogonal symmetry and periodic boundary conditions are applied in three dimensions. The computational boxes contain up to 128 surfactant molecules and counterions plus up to several thousand water molecules. The Ewald summation method was used to handle long-range Coulomb interactions. The equations of motion were integrated using a Verlet leapfrog scheme [20] and a time step of 2 fs.

The surfactant double layer was constructed by putting the surfactants tail-to-tail on a square lattice in the y–z plane. Then the counterions and water molecules were added. The surface areas per HG are 30.4 and 45.2 Å^2 for the erucate and the EHAC surfactants,
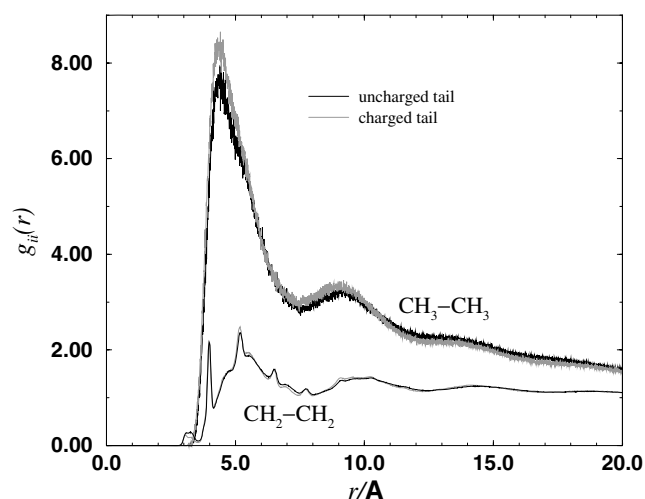
Figure 7. The pair correlation function $g_{ii}(r)$ of the $i = CH_2$ carbon atoms (lower curves) and the $i = CH_3$ carbon atoms (upper curves), for both the charged (grey) and the uncharged (black) model of the erucate tail for the 8×8 surfactant bilayer systems.

Table 2. Summary of surfactant parameters used with the simulation running times: N: number of surfactant molecules; N_a: number of atoms per surfactant molecule; N_w: number of SPC water molecules; N_{tot}: total number of atoms; Δt_1: time step of the first minimizing NVT simulation for 20 000 steps; t_{NVT}: running time of the second NVT simulation; t_{NpT}: running time of the NpT simulation.

Surfactant	Bilayer	N	N_a	N_w	N_{tot}	Δt_1 (fs)	t_{NVT} (ps)	t_{NpT} (ps)
Erucate	5×5	50	68	432	4 746	0.001	400	300
	8×8	128	68	1106	12 150	0.02	100	274
EHAC	5×5	50	86	567	6 051	0.01	200	300
	8×8	128	86	1966	17 034	0.05	140	200

respectively. The different values reflect their different HG sizes, quantified by the radii of gyration R_g, with the values $R_g = 0.86$ Å for the erucate and $R_g = 2.41$ Å for the EHAC. The systems were allowed to equilibrate in the constant-NVT ensemble. This was done carefully in two stages (see table 2). First, about 20 000 time steps of 0.001–0.05 fs were performed at a temperature $T = 100$ K to remove spurious strain. This was followed by about 100 000 steps of 2 fs. The temperature was maintained at 300 K using an NVT Nosé–Hoover thermostat [35].

Following NVT equilibration, the subsequent production runs were carried out in the isothermal–isobaric (NpT) ensemble for about 300 ps. The pressure was kept constant by using a Melchionna modification of the Hoover algorithm [36] in which the equations of motion involve a Nosé–Hoover thermostat and a barostat in the same way. Atomic coordinates were stored every 0.1 ps. Structural properties of the membrane, such as radial distribution functions and density profiles, were obtained from ensemble averages. Details of the simulation runs, including numbers of molecules used, equilibration and production run lengths, are given in table 2.

7. Results: membrane structure

The structure of the membranes can be characterized by calculation of various radial distribution functions $g(r)$ and density profiles $\rho(x)$ along the normal x to the membrane surface. The density distributions of the HG centres of mass, the carbon atoms in the membrane core, counterions and water molecules, with respect to separation of the particles from the centre plane of the membrane, are shown in figure 4.

These figures show that there is a significant amount of water penetration into the membrane core. The HG and counterion profiles follow the water profiles near the membrane surface, as might be expected. This is in good agreement with Klein's simulations of octanoate micelles [29]. Interestingly, in a recent simulation of a DPPC bilayer [25], a similar degree of water penetration was observed, but described as not entering the hydrophobic core. Closer inspection of our profiles shows that the HG and counterion distributions for the erucate are sharper than for the EHAC. The EHAC distributions show oscillations of the HG and counterion profiles even in the middle of the water box. This suggests that the membrane surfaces may no longer be planar. That this is indeed the case can be observed from snapshots of the last frames of the simulations; see figure 5. These snapshots also show qualitatively that the erucate carbon tails are highly ordered, whereas the EHAC tails are highly disordered. This effect can be quantified by studying the head–tail correlation. The head–tail correlation is calculated from the correlation of the normalized distance vectors $\vec{s}_i$ between HG and terminal carbon atom in the tail for surfactant i: $\langle \sum_{i<j} \vec{s}_i \cdot \vec{s}_j \rangle / (\frac{N(N-1)}{2})$, where N is the number of surfactants in one leaflet. If this quantity is unity then the tails are fully correlated; for the value of zero they are completely uncorrelated. We obtain in the erucate case a value of 0.93, i.e. the heads and tails are highly correlated. The EHAC surfactant tails yield a correlation value of 0.62, which means that the tails are only weakly correlated. A weak head–tail correlation seems to coincide with the membrane surface becoming unstable.

The radial distribution functions $g_{ii}(r)$ for $i = $ >CH$_2$ and $i = $ –CH$_3$ carbon atoms are shown in figure 6. The >CH$_2$ $g(r)$ is similar to experimental data for liquid alkanes and to the simulation data for octanoate molecules in water [29]. This $g(r)$ shows both *inter*molecular and *intra*molecular features: the satellite peaks at 4.3, 5.0 and 6.2 Å are due to correlations between carbon atoms in the same chain.

From the simulation snapshots in figure 8, we can observe that there is a correlation between the spatial distribution of the HGs and the double bonds in the hydrocarbon tails. In order to quantify this, the probability distributions were calculated for the *intra*chain separations between the HGs on the one hand and the double bonds/terminal –CH$_3$ groups on the other hand; see figure 9. The sharp peak in the erucate (HG–C=C) profile at large r is due to the fully extended (all-*trans*) chain conformation. The erucate profile is very similar to the octanoate profile discussed earlier [29]. The EHAC surfactant shows broader peaks at smaller distances, corresponding to a stronger tendency to 'fold back' (chains with one or more *gauche* defects). In general the profiles for C=C are sharper than for –CH$_3$, indicating that the first part of the chain is less flexible. We have also performed simulations of surfactant molecules where the hydrocarbon chain has been chopped at the double bond. The results of these simulations, which will be presented in detail elsewhere [33], show very different behaviour. This means that coarse-graining in this fashion should be regarded with caution.

From the simulation snapshots in figure 5, we can observe that for the erucate, the counterions are in close contact with the surfactant HGs, more so than in the case of the EHAC surfactant. In order to quantify this, the radial distribution function $g_{ij}(r)$ between the HG centres of mass i and the counterions j was calculated; see figure 10. In the case of the erucate, there is a bimodal distribution for the contact ions ($r < 4.3$ Å). The peaks at 2.65 and
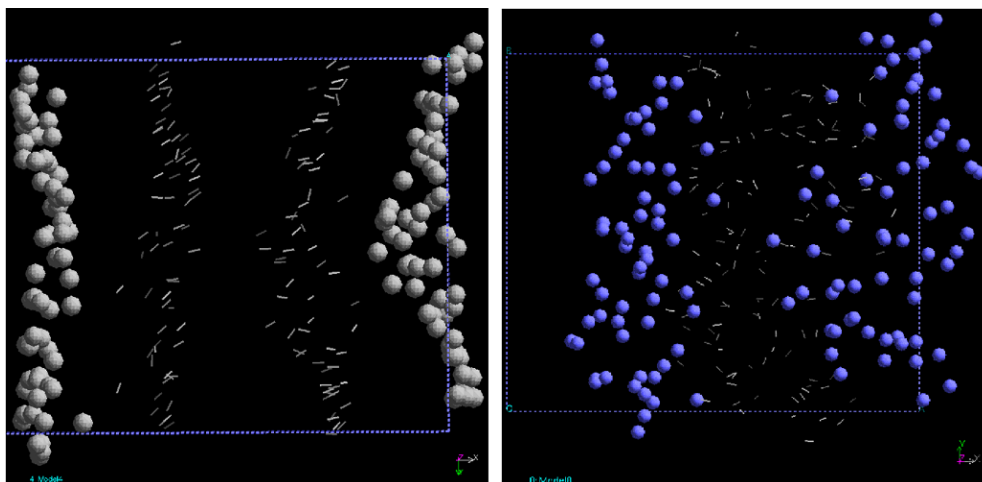
**Figure 8.** Simulation snapshots of HGs and double bonds for both erucate (left) and EHAC (right).
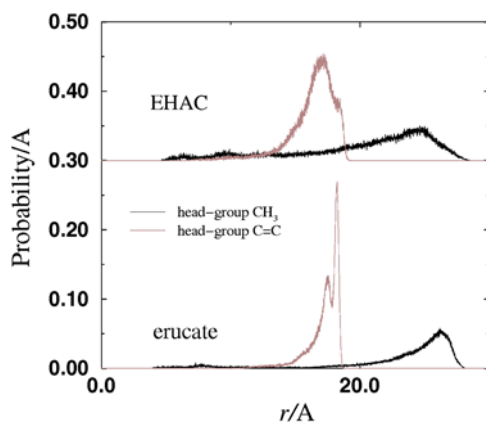
Figure 9. Probability distributions for the distances of C=C (grey) and –CH$_3$ (black) to the surfactant HG.

3.5 Å both represent sodium ions which are in direct contact with the surfactant HGs. In this case we have an example of counterion condensation. The situation is different for the EHAC, where there is no direct contact between ions and HGs (first peak at 5.3 Å). This is in line with the fact that the charge on the positively charged EHAC HG is more distributed and diffuse than the negative charge on the erucate HGs, causing the counterions to be distributed more diffusely. Note that ^{23}Na$^+$ quadrupole resonance experiments are sensitive to changes in the counterion distribution. It should therefore be possible to verify the simulation prediction by experiment. The erucate simulation snapshot in figure 11 confirms the picture of counterion condensation: it appears that the sodium ions are closely correlated with the oxygen atoms of the carboxylate HGs. A NMR study of chemical shift and quadrupolar relaxation of ^{23}Na$^+$ in octanoate solutions confirms this picture: this study suggested that the counterions have a preferred location between amphiphilic HGs [37]. Note that our intermolecular potential model does not allow for dynamic induced polarization of the surfactant molecules. This
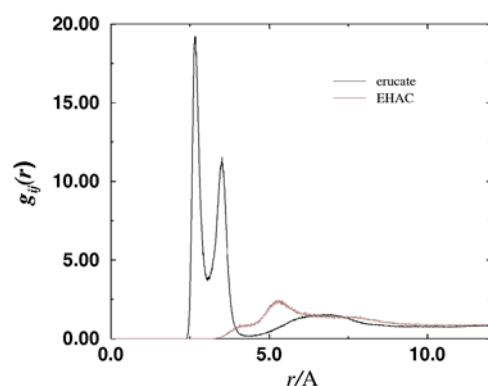
Figure 10. Radial distribution functions $g_{ij}(r)$ for HGs i and counterions j for both erucate (black) and EHAC (grey).
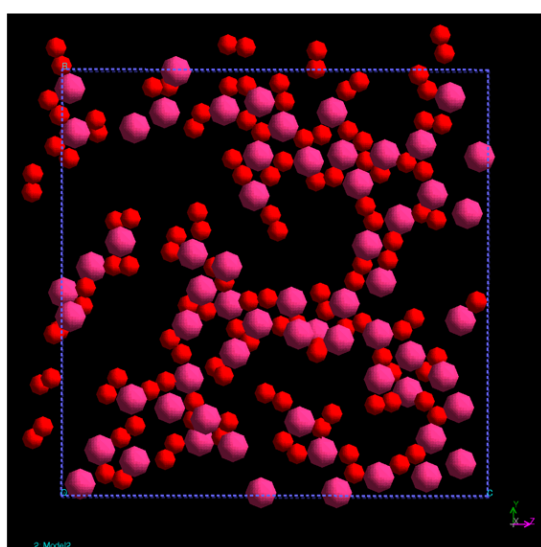

Figure 11. A simulation snapshot (perpendicular to the lamellar surface) of one membrane leaflet for the oxygen atoms in the erucate HGs (smaller spheres) and counterions (larger spheres).

has been shown to have a significant effect on the structure of the micellar aggregates in a simulation study of sodium octanoate micelles [38].

In figure 12, the $g_{ii}(r)$ for the counterions are shown. The $g_{ii}(r)$ of the Na$^+$ ions in the erucate systems are highly structured, compared with those for a solution of these ions in water. The ratio of the positions of the first peak (4.0 Å) and the second peak (6.9 Å) is approximately $\sqrt{3}$. This suggests that the ions can be described as a 2D liquid with short-ranged hexagonal packing adsorbed on the micellar surface. The ratio between first and second peak is much smaller than $\sqrt{3}$ in the case of the EHAC counterions, which suggests that a different mechanism is at work.

The $g_{ii}(r)$ of the HG i is shown in figure 12(a) and is normalized to the two-dimensional ideal-gas density of the layer $\rho_{id} = N/2A$, where A is the membrane layer surface. Compared with the $g(r)$ of a simple liquid, there is significant structure in the distribution function in the
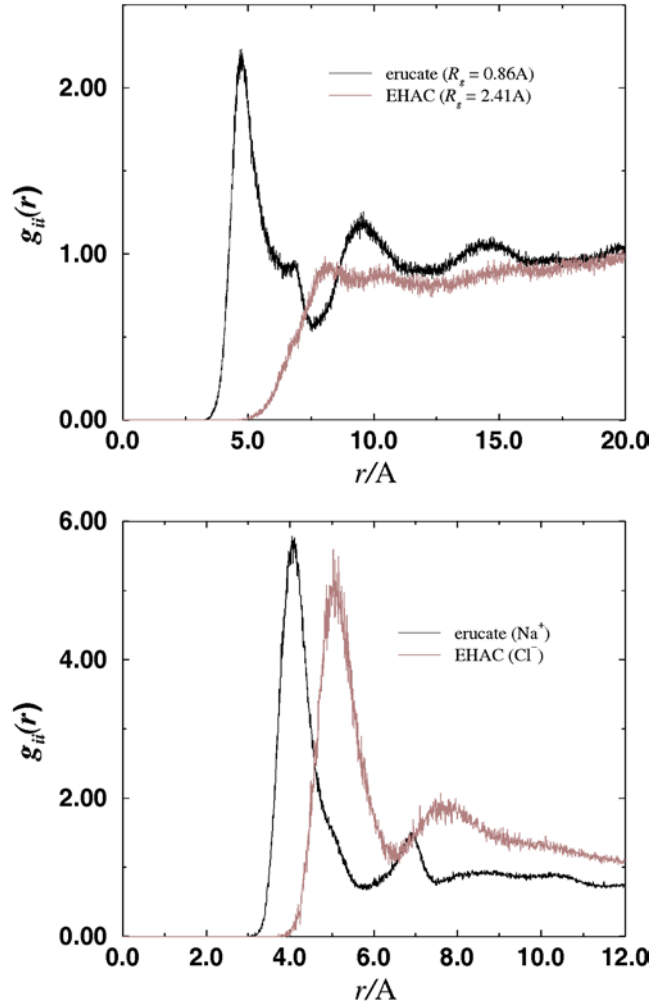
Figure 12. Radial distribution functions $g_{ii}(r)$ for pairs of HGs (top) and counterions (bottom) for both erucate (black) and EHAC (grey).

erucate case, and it is justified to discuss the $g(r)$ in terms of a strongly correlated 2D fluid. In a qualitative sense, strong correlations between the erucate HGs imply that these HGs have strong interactions. The $g(r)$ for EHAC does not show any very considerable correlations, which implies that the HG interactions are weaker than for the erucate case.

8. Isothermal compressibility

We have also calculated the isothermal compressibility which represents a macroscopic quantity of the membrane and is readily accessible experimentally (see e.g. [39]). For a bulk fluid, the isothermal compressibility β_T can be calculated from the volume fluctuations in the NpT ensemble considered [20]:

$$\beta_T = \frac{1}{\langle V \rangle} \frac{\langle V^2 \rangle - \langle V \rangle^2}{k_B T},\tag{9}$$

Table 3. Compressibilities of the membrane β_T^m and the water slab β_T^w, calculated from 5×5 bilayer systems.

Surfactant	β_T^m (10^{-10} Pa^{-1})	β_T^w (10^{-10} Pa^{-1})
Erucate	5.2	7.1
EHAC	15.9	22.2

where V denotes the volume of the system. Results for these compressibilities, as obtained from 5×5 bilayer systems, are presented in table 3. We distinguish between the compressibility of the water slab β_T^w and of the membrane β_T^m. We obtain both values by calculation of their corresponding volume fluctuations according to equation (9). The volumes of the water and the surfactant molecules were calculated for every configuration by triangulating the HG positions. Note that in the present approach, the volume fluctuations of water and membrane are coupled. Therefore they are not directly related to real physical compressibilities, but represent an estimate of the total compressibility. For a more thorough technique for accessing the membrane compressibility, we refer the reader to [40].

The compressibility shows large differences between the surfactant systems considered. The erucate surfactant has a value of β_T^m of the order of 5×10^{-10} Pa^{-1}, which corresponds with the value of β_T for micellar solutions with different micellar shapes, as measured in experiments [41]. Also the compressibility of the water phase β_T^w is of the same order as the literature value for pure water [4]. This is different in the EHAC case where the values obtained for β_T^m and β_T^w are three times higher. In this case, the water penetration is deep into the membrane (see figure 4). This means that the determination of the compressibilities suffers from finite-size effects caused by the extended water–membrane interfaces. Furthermore, the statistical error itself in the different system size fluctuations is large, such that our determination of compressibilities is only semi-quantitative.

9. Conclusions

In conclusion, we have performed extensive molecular dynamics simulations which resolve the full atomistic detail in order to determine how the structure of the lamellar phase of viscoelastic surfactant solutions depends on the HG chemistry of the surfactants. This problem is critical for the molecular design of responsive oilfield fluids based on these materials. Two different cases were studied in detail, namely carboxylate and bis(hydroxyethyl) methylammonium HGs. The membrane structure was quantified by the diagnostics of pair correlation functions and density distribution functions [19]. Large differences in bilayer structure were found between the two cases, which we attribute to different degrees of counterion condensation on the HGs which then couple to the effective head–head interactions and even to the structure of the tail molecules. Our simulation predictions can in principle be verified by experiments, e.g. by means of quadrupole resonance. The general conclusion of our studies is that even relatively small changes in the chemistry of the surfactants can have a dramatic effect on the membrane structure. This implies that one has to be careful in using highly coarse-grained models to predict macroscopic quantities quantitatively. Note that recent simulations by Klein *et al* [38] indicate that the inclusion of dynamic induced polarization of the surfactant HGs may change the structural properties of the micellar aggregates as well as the counterion condensation effects observed.

An initial attempt has been made to link these molecular simulations to their macroscopic behaviour by calculating the membrane compressibility. The effect of HG changes on the

this parameter provides, in principle, a route to predicting changes in bulk phase behaviour. However, more extensive simulations are required to achieve this.

Future work should include different HGs and tails. In fact, we have collected data for two further HGs as well as different tails which will be presented elsewhere [33]. Also the case of cylindrical and spherical micelles, which requires larger simulation sizes, should be addressed. Clearly more simulation work is needed to resolve the consequences of subtle changes in surfactant molecular structure.

Acknowledgments

References

[1] Coveney P V and Humphries W 1996 *J. Chem. Soc. Faraday Trans.* **92** 831
[2] Black S N, Bromley L A, Cottier D, Davey R J, Dobbs B and Rout J E 1991 *J. Chem. Soc. Faraday Trans.* **87** 3409
[3] Davey R J, Black S N, Bromley L A, Cottier D, Dobbs B and Rout J E 1991 *Nature* **353** 540
[4] Boek E S, Coveney P V and Skipper N T 1995 *J. Am. Chem. Soc.* **117** 12 608
    Boek E S, Coveney P V and Skipper N T 1995 *Langmuir* **11** 4629
[5] Bains A S, Boek E S, Coveney P V, Williams S J and Akbar M V 2001 *Mol. Simul.* **26** 101
    Boek E S, Coveney P V, Craster B and Reid P 1998 Chemicals in the oil industry *Proc. 6th Int. Symp. on Chemistry in the Oil Industry* (Cambridge: Royal Society of Chemistry)
[6] Samuel M *et al* 1997 *Proc. SPE Annu. Tech. Conf.; Proc. SPE* **38622** 553
[7] Kesavan S and Prud'homme R K 1992 *Macromolecules* **25** 2026
[8] Menge U, Lang P and Findenegg G H 1999 *J. Phys. Chem.* B **103** 5768
[9] Magid L J, Han Z, Li Z and Butler P D 2000 *J. Phys. Chem.* B **104** 6717
[10] von Berlepsch H, Harnau L and Reineker P 1998 *J. Phys. Chem.* B **102** 7518
[11] Hassan P, Candau S J, Kern F and Manohar C 1998 *Langmuir* **14** 6025
[12] Callaghan P T 1999 *Rep. Prog. Phys.* **62** 599
[13] Oda R, Panizza P, Schmutz M and Lequeux F 1997 *Langmuir* **13** 4551
[14] Maillet J-B, Lachet V and Coveney P V 1999 *Phys. Chem. Chem. Phys.* **1** 5277
[15] Rouault Y 1999 *J. Chem. Phys.* **111** 9859
[16] Coveney P V *et al* 1999 *J. Mod. Phys.* C **9** 1479
[17] Cates M E 1988 *J. Physique* **49** 1593
[18] Raghavan S R and Kaler E W 2001 *Langmuir* **17** 300
[19] Hansen J-P and McDonald I R 1986 *Theory of Simple Liquids* 2nd edn (London: Academic)
[20] Allen M P and Tildesley D J 1987 *Computer Simulation of Liquids* (Oxford: Clarendon)
[21] Ben-Shaul A and Gelbart W M 1994 *Micelles, Membranes, Microemulsions and Monolayers* (New York: Springer)
[22] Helfrich W 1973 *Z. Naturf.* c **28** 693
[23] Safran S 1994 *Statistical Thermodynamics of Surfaces, Interfaces and Membranes* (Reading, MA: Addison-Wesley)
[24] Goetz R, Gompper G and Lipowsky R 1999 *Phys. Rev. Lett.* **82** 221
[25] Lindahl E and Edholm O 2000 *J. Chem. Phys.* **113** 3882
[26] Marrink S J and Mark A E 2001 *J. Phys. Chem.* B **105** 6122
[27] Landau L D and Lifshitz E M 1970 *Theory of Elasticity* 2nd edn (New York: Pergamon)
[28] May S, Bohbot Y and Ben-Shaul A 1997 *J. Phys. Chem.* B **101** 8648
[29] Watanabe K and Klein M 1991 *J. Phys. Chem.* **95** 4158
[30] Berendsen H J C, Postma J P M, van Gunsteren W F and Hermans J 1981 *Intermolecular Forces* ed B Pullman (Dordrecht: Reidel)

[31] Mayo S L, Olafson B D and Goddard W A III 1990 *J. Phys. Chem.* **94** 8897
[32] Stewart J J P 1990 MOPAC 6.0, QCPE No 445
[33] Boek E S, Jusufi A, Löwen H and Maitland G C 2002 in preparation
[34] http://www.dl.ac.uk/TCS/Software/DL_POLY/main.html
[35] Hoover W G 1985 *Phys. Rev.* A **31** 1695
[36] Melchionna S, Ciccotti G and Holian B L 1993 *Mol. Phys.* **78** 533
[37] Lindblom G, Lindman B and Tiddy G T J 1978 *J. Am. Chem. Soc.* **100** 2299
[38] Shelley J C, Sprik M and Klein M L 1993 *Langmuir* **9** 916
[39] Lis L J *et al* 1982 *Biophys. J.* **37** 667
[40] Goetz R and Lipowsky R 1998 *J. Chem. Phys.* **108** 7397
[41] Kudryashov E, Kapustina T, Morrissey S, Buckin V and Dawson K 1998 *J. Colloid Interface Sci.* **203** 59
     Wang L and Verrall R E 1994 *J. Phys. Chem.* **98** 4368
     Kawaizumi F, Kuzuhara T and Nomura H 1998 *Langmuir* **14** 3749
     Amararene A, Gindre M, Le Huérou J-Y, Urbach W, Valdez D and Waks M 2000 *Phys. Rev.* E **61** 682
     Gonzáles-Gaitano G, Crespo A and Tardajos G 2000 *J. Phys. Chem.* B **104** 1869
     Gonzáles-Gaitano G, del Castillo J L, Czapkiewicz J and Rodríguez J R 2001 *J. Phys. Chem.* B **105** 1720
     Antelmi D A and Kékicheff P 1997 *J. Phys. Chem.* B **101** 8169
     Hianik T, Haburcák M, Lohner K, Prenner E, Paltauf F and Hermetter A 1998 *Colloids Surf.* A **139** 189